Plasma distributions observed in a 2.45 GHz hydrogen discharge

O D Cortázar[1], A Megía-Macías[2], O Tarvainen[3], A Vizcaíno-de-Julián[2] and H Koivisto[3]

[1] Department of Applied Mechanics - INEI, University of Castilla-La Mancha, ETSII, Av. Camilo Jose Cela s/n, 13071-Ciudad Real, Spain
[2] ESS Bilbao Consortium, Polígono Ugaldeguren-III Pol. A 7B, 48170-Zamudio, Vizcaya, Spain
[3] Department of Physics, University of Jyväskylä, PO Box 35 (YFL), 40500. Jyväskylä, Finland

E-mail: daniel.cortazar@uclm.es

Abstract
The existence of various spatial distributions of hydrogen plasma in a pulsed 2.45 GHz microwave discharge is demonstrated. The data has been obtained through optical emission diagnostics utilizing an ultra-fast CCD camera system with multi-channel plate (MCP) intensifiers, and a wavelength-filtered photodiode recording temporal light emission signals of hydrogen atoms and molecules. It has been observed that the magnetic field topology and strength are determining the transitions between different plasma patterns and spectral saturation times while neutral gas pressure and microwave power show a weaker influence on the profiles but affect the emitted light intensity.

Keywords: ECR, plasma source, ultra-fast pictures

(Some figures may appear in colour only in the online journal)

1. Introduction

Ultra high speed photography by image intensified gated cameras has been an important diagnostics tool during recent decades especially for hot and dense plasmas with intense light emission such as Z-pinches, plasma focus and exploding wire [1–3]. The obtained pictures yield information about plasma density distributions and their time evolution as well as its interaction with magnetic fields. However, only a few studies of spatial and/or temporal light emission have been conducted [4–7] in the case of electron cyclotron resonance (ECR) plasmas sustained at frequencies up to 14 GHz. Such discharges operated at 2.45 GHz are widely used as proton ion sources for high power accelerators [8]. Studying the effect of various plasma parameters on their light emission characteristics provides information e.g. on the microwave–plasma coupling. Such information can be used for optimizing the performance of microwave ion sources in terms of plasma density and atomic to molecular ion species fraction.

2. Experimental setup

The experiments have been performed on TIPS (Test-bench for Ion-source Plasma Studies): a 2.45 GHz plasma generator running at 50 Hz, 10% duty factor in pulsed mode with hydrogen. The device is driven by a 3 kW adjustable power magnetron. A detailed description of the plasma generator has been published recently in [9, 10] but, important modifications have been introduced on it to obtain frame pictures of full plasma volume [11]. Figure 1 shows a cross section view of the system. The aluminum plasma chamber (*a*), with 113 mm length by 85 mm diameter, is limited by the microwave system (right) and the diagnostic port (left). A ridged wave guide coupler (*b*) is used for maximizing the electric field value at the center of the plasma chamber [12]. Hydrogen flows into the chamber through the inlet port (*c*) while pressure values inside the plasma chamber are measured by a penning type gauge connected to the gas pressure inlet (*d*). No differences have been observed on the pressure readings due to magnetic field as the gauge is protected by the magnetic steel yoke shaping the magnetic field. A 10 mm thick quartz window (*e*) separates the vacuum enclosure from the microwave
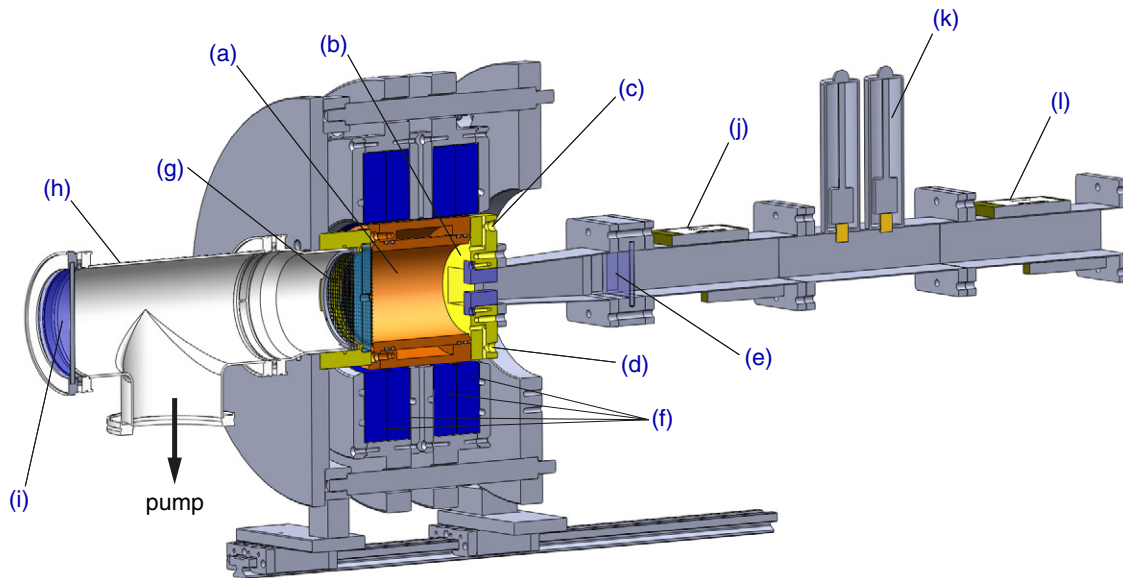
Figure 1. A cross-sectional view of the plasma source: (*a*) plasma chamber, (*b*) microwave coupler, (*c*) gas inlet, (*d*) vacuum gauge port, (*e*) quartz window, (*f*) coil pancakes, (*g*) optical window with shielding grids, (*h*) vacuum tee, (*i*) quartz viewport, (*j*) and (*l*) bidirectional coupler and (*k*) two-stub tuner.

driver system. A set of four coaxial coils (*f*) arranged in two pancakes with independently adjustable currents and a positioning mechanism produces different magnetic field profiles. A Boron Nitride disk is placed at the microwave injection side in order to prevent plasma leakage into the coupler.

The optical window that plays the role of a transparent plasma electrode is also shown in figure 1(*g*). Two meshes, of 2.5 mm square structure made of 0.25 mm tungsten wires are placed at both sides of a 10 mm thick quartz window that has a cylindrical hole of 7 mm diameter on axis. Both meshes are grounded to the plasma chamber. Such design meets three important criteria: to obtain a projected image of the whole plasma chamber volume, to pump gas through the centered hole and to provide a conducting surface, which preserves the boundary condition of a typical plasma generator minimizing the leakage of the microwaves into the pumping chamber. The late has been verified with a measurement of non-ionizing radiation with a specific radiometric device by NARDA mod. NBM-550. No differences has been observed on general plasma behavior respect to a solid aluminum plasma electrode. The pumping system is connected to the plasma generator through a standard ISO DN 100 tee (*h*) that allows to place a quartz view port (*i*) on the optical axis of the discharge chamber. A two-stub tuner (*k*) is used for fine impedance matching and bidirectional-couplers (*j*) and (*l*) give readings of incoming and reflected power from magnetron and plasma respectively.

Black and white images are acquired with an Intensified Frame CCD Camera System made by Cordin Corp. (model 220A). A Pentax 67 × 150 mm telephoto lens with a focus ring to reduce the minimum focus distance is attached to the camera. A pulse delay generator is used for synchronizing the camera trigger with the microwave pulses and, hence, guaranteeing that images are acquired after the ignition transient (typically
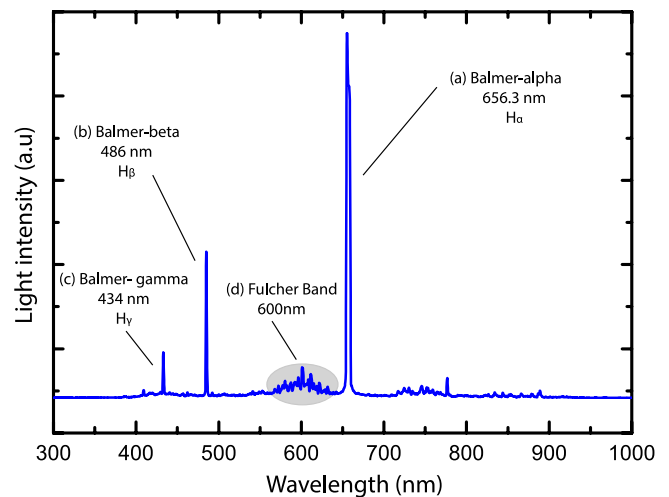

Figure 2. Typical integrated time spectrum obtained by a fiber optics spectrometer where Balmer series and Fulcher band are shown.

at the middle of the microwave pulse). Typical exposure time used in this study is 1 μs. The MCP and CCD gains can be adjusted depending on the light intensity to optimize the images.

The auxiliary diagnostics include bidirectional couplers recording incident and reflected power signals and an optical viewport coupled either with a visible light spectrometer (by THORLABS model CCS200/M) recording optical emission spectra (200–1000 nm) or a wavelength-filtered photodiode recording temporal light emission signals. These complimentary optical diagnostics are necessary since the integration time of the spectrometer exceeds the microwave pulse length. Figure 2 shows a typical visible light spectrum obtained with the spectrometer. The Balmer series alpha (*a*) at 656.3 nm, beta (*b*) at 486.1 nm, gamma (*c*) at 434.1 nm lines and Fulcher band (*d*) are clearly indicated.

The visible light emission from hydrogen plasma is due to the excitation of neutral hydrogen atoms and molecules by electron impact from level q to level p and the decay into level k by spontaneous emission resulting in line emission pk. The hydrogen Balmer series corresponds to the transitions from the excited states of atomic hydrogen with the primary quantum number $n_p > 2$ to the excited state with $n_k = 2$. Balmer-alpha radiation at 656.3 nm is emitted when $n_p = 3$ i.e. it is the primary transition within the Balmer-series. For Balmer-beta the corresponding numbers are 486.1 nm and $n_p = 4$. It is of note that emission within the Balmer series is followed by emission in VUV-range at 121 nm corresponding to the Lyman alpha transition. The $n = 3$ and $n = 4$ states are populated by atomic excitation and dissociative excitation of H_2-molecules by electron impact. The relative importance of these processes depends on the densities of neutral atoms and molecules as well as the distribution of electron energies. In low temperature plasmas (Te on the order of 10 eV) the rate for atomic excitation is typically greater by more than an order of magnitude [13]. However, the exact ratio of the two excitation channels depends on the vibrational distribution of the molecules. The Fulcher-band emission around 600 nm corresponds to the molecular triplet transition $d\,^3\Pi_u \to a\,^3\Sigma_g^+$ with a further transition (emission in UV) $a\,^3\Sigma_g^+ \to b\,^3\Sigma_u^+$ to a repulsive state (molecular continuum, see for example [14]). Thus, Fulcher-band emission indicates dissociation of the emitting molecule [15].

Since the radiative lifetimes of the excited states resulting to light emission within the Balmer series (and Fulcher-band) are on the order of 10^{-7} s (and 10^{-8} s) [14, 16], i.e. shorter than the time between consecutive excitation reactions, it can be assumed that the plasma is in so-called corona regime. This allows us to link the measured atomic light emission with ionization since the ratios of the excitation cross sections (e.g. $1s \to n = 3$) to ionization cross section are well-defined. Furthermore the ratios of the atomic excitation cross sections to different excited states can be used for interpreting the data taken with the spectrometer. Figure 3 shows the atomic excitation cross sections [17] from the ground state to $n_p = 3$ and $n_p = 4$ states, the ground state ionization cross section and the ratios of the given reactions as a function of impacting electron energy. It can be seen that increasing electron average energy implies increasing H_β/H_α-ratio and increasing ionization rate at electron energies typical for the microwave discharge [10, 11, 18]. It must be emphasized that the given assumption (corona regime) fails if the metastable $2s$-state of hydrogen atoms is heavily populated since the cross sections and threshold energies of the excitation and ionization reactions are significantly different in comparison to the ground state [17]. Unfortunately the relative population densities of the $1s$- and $2s$-states are unknown. Using the molecular light emission to determine the plasma properties is even more complicated as the reaction cross sections depend heavily (orders of magnitude) on the vibrational distribution of the molecules [17], which is unknown as well.
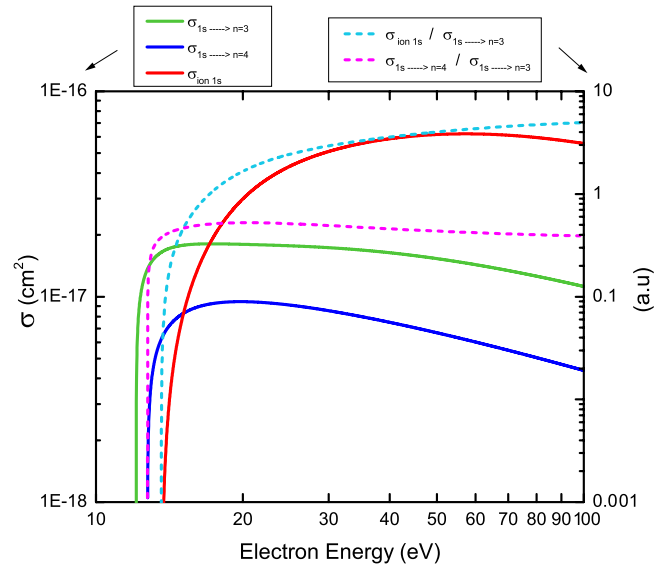

Figure 3. Atomic excitation cross sections from the ground state to $n_p = 3$ and $n_p = 4$ states, the ground state ionization cross section and the ratios of the given reactions as a function of impacting electron energy. Cross sections are taken from [15].

3. Results

Different distributions of light emission have been recorded in a wide range of experimental conditions. Hydrogen pressures ranging from 3.8×10^{-3} to 8.6×10^{-3} mb and incident powers from 300 to 1500 W were used in the experiments. The corresponding range of reflected power was 5–70%. Figure 4 shows the collection of various plasma light emission profiles (projections) observed during the experiments. All photos have been obtained with a single shot and exposure time of $1\,\mu$s. The light emission profiles typically evolve during the plasma ignition transient. All pictures presented in this article have been obtained after the profile is well established. A synchronization scheme with a delay generator triggered by the incoming power signal has been used for timing. Note that the images are originally obtained in B&W but have been transformed by software into a representation where red corresponds to highest intensity (saturated white) and blue the lowest (deep black). Eight reproducible patterns have been recognized emerging at certain combination of source parameters, i.e. magnetic field profile, gas pressure and incident/reflected microwave power. Note that in figure 4 the plasma chamber diameter is marked by a dark and fine blue circular line especially visible in the cases (*a*), (*b*), (*d*), (*e*) and (*g*). The shadow produced by the fiber optics collimator of the spectrometer can be observed in the lower left corner of almost all pictures. The authors have chosen descriptive names for each pattern as suggested by their apparent shapes: figure 4(*a*) *column*, figure 4(*b*) *hourglass*, figure 4(*c*) *slug*, figure 4(*d*) *flower*, figure 4(*e*) *full chamber*, figure 4(*f*) *ring*, figure 4(*g*) *Yin-Yang* and figure 4(*h*) *donut*.

It has been observed that the magnetic field profile is determining the transitions between different patterns and saturation times while neutral gas pressure and microwave
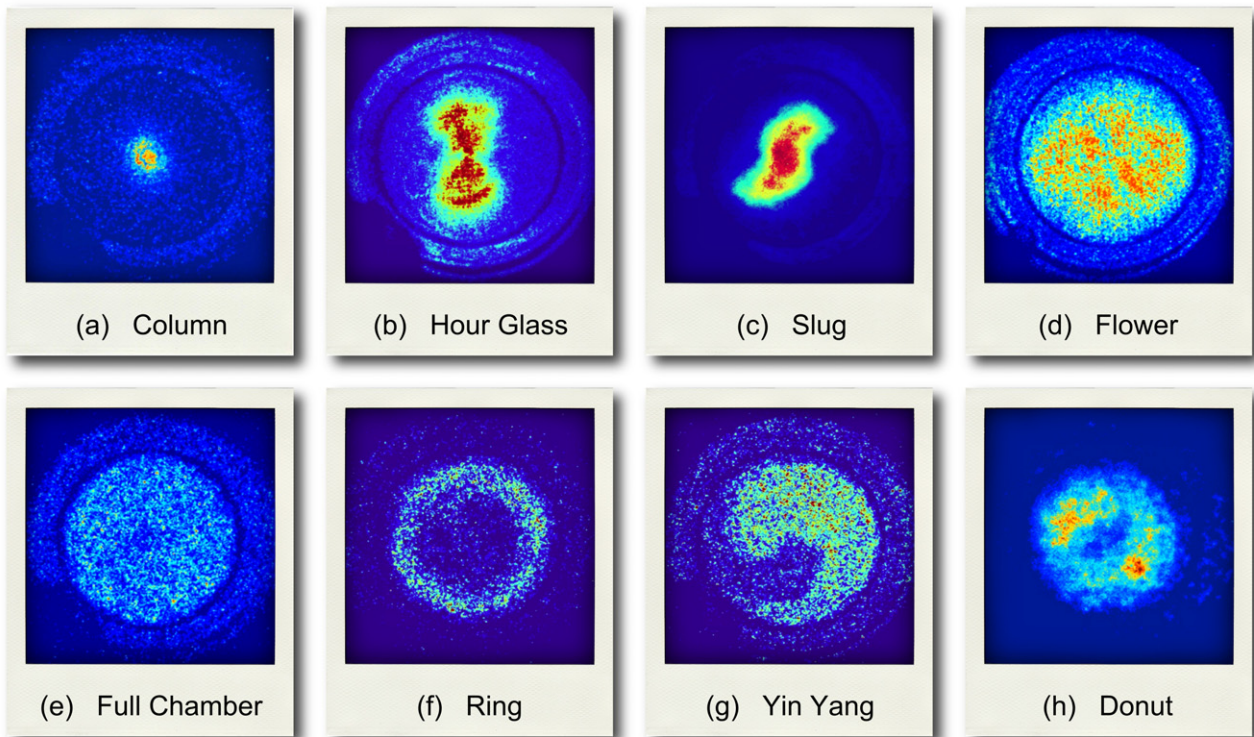
Figure 4. Different plasma distributions observed during the experiments. False color calibration is used where red corresponds to highest intensity and blue the lowest.

power show a weaker influence on the profiles but affect the light intensity instead.

The ratios between spectral emission lines of atoms and molecular band as well as their saturation times show remarkable differences between the plasma distributions. The set of pictures in figure 4 has been arranged in two groups (*a*)–(*c*) and (*d*)–(*h*) depending the emission intensity. It is of note, however, that some emission profiles appear in wide range of intensities depending on the magnetic field profile.

In the following subsections we describe the experimental conditions corresponding to each plasma distribution. The 2D magnetic field profiles have been simulated with FEMM 4.2 [19]. The simulations have been validated by measurements using a vectorial magnetic probe. The *B-field* configurations shown in the following cases correspond to experimental conditions where plasma behavior is stable and reproducible.

3.1. On-axis column

Figure 5 shows a typical picture in which the plasma distribution is concentrated on the axis of the plasma chamber (*a*), Hereafter the distribution is referred as *column*. A 3D map of the light intensity is shown below the 2D projection. The corresponding visible light spectra, temporal light signals recorded with the diode and magnetic field profiles are also presented. The magnetic field distributions are shown for the volume inside the plasma chamber, where the axis being the horizontal dashed line in the middle of the field density

plot. The microwaves are injected from the left and the transparent electrode is placed on the right. The broken curves represent either the ECR surfaces (87.5 mT) or $B_{ECR}/2$ surfaces (43.8 mT). Three different magnetic filed profiles have been observed to yield the column distribution, two of them fulfilling the ECR-condition and one being an off-resonance case.

In the first two cases the light intensity is high and the spectrum is dominated by emission lines of hydrogen atoms. In the last case the magnetic field strength is significantly lower resulting to low-intensity light emission with increased (relative) fraction of molecular emission. It is worth noting that in the case of high intensity column distribution the intensity of atomic emission increases throughout the 2 ms microwave pulse i.e. the steady-state of light emission is not reached.

3.2. Hourglass

Figure 6 shows a typical picture with the plasma distribution denominated *hourglass*(*a*) characterized by a waist on the axis with two symmetric lobes aligned with the microwave electric field. Only one kind of visible light emission spectrum has been observed under four different magnetic profile distributions. Although H_α is still dominant, the relative intensity of higher order Balmer lines (H_β and H_γ) is higher in comparison to the previous case (column) indicating higher electron temperature for the *hourglass*. The saturation time of the light emission signals is also shorter (in comparison to the column) in the cases of the magnetic field fulfilling the resonance condition.
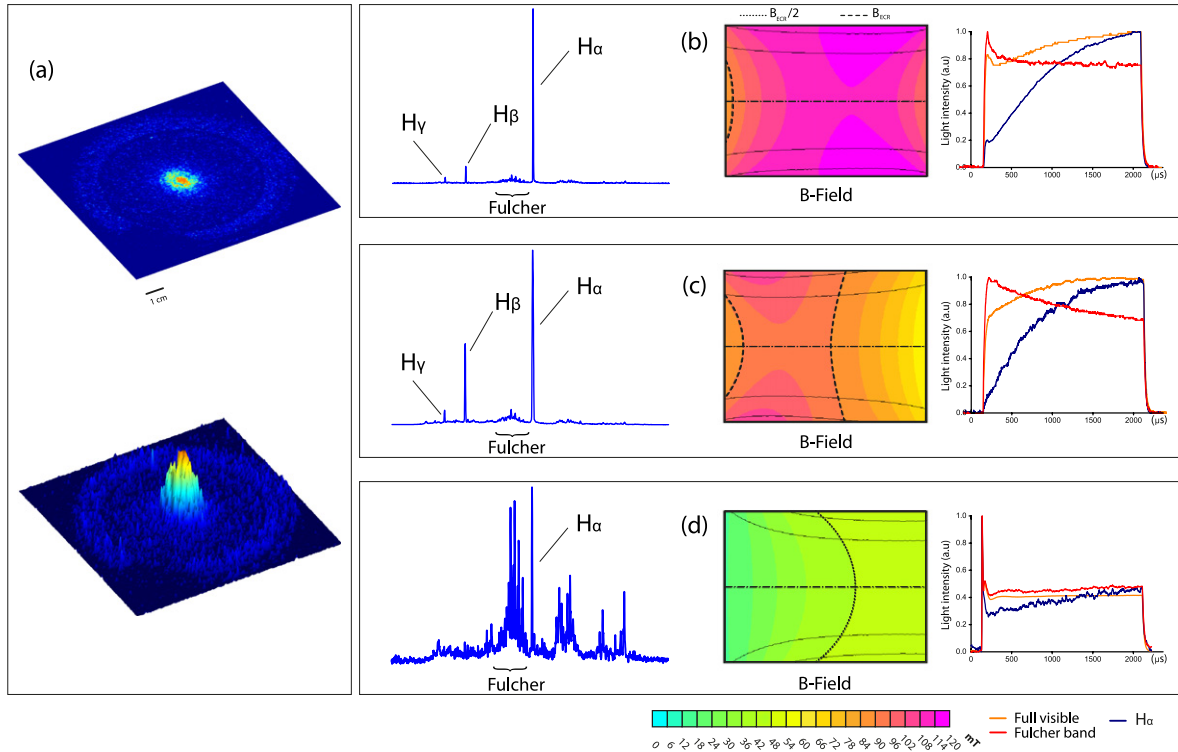
Figure 5. Column distribution with corresponding visible light spectra, filtered diode signals and magnetic field profiles.
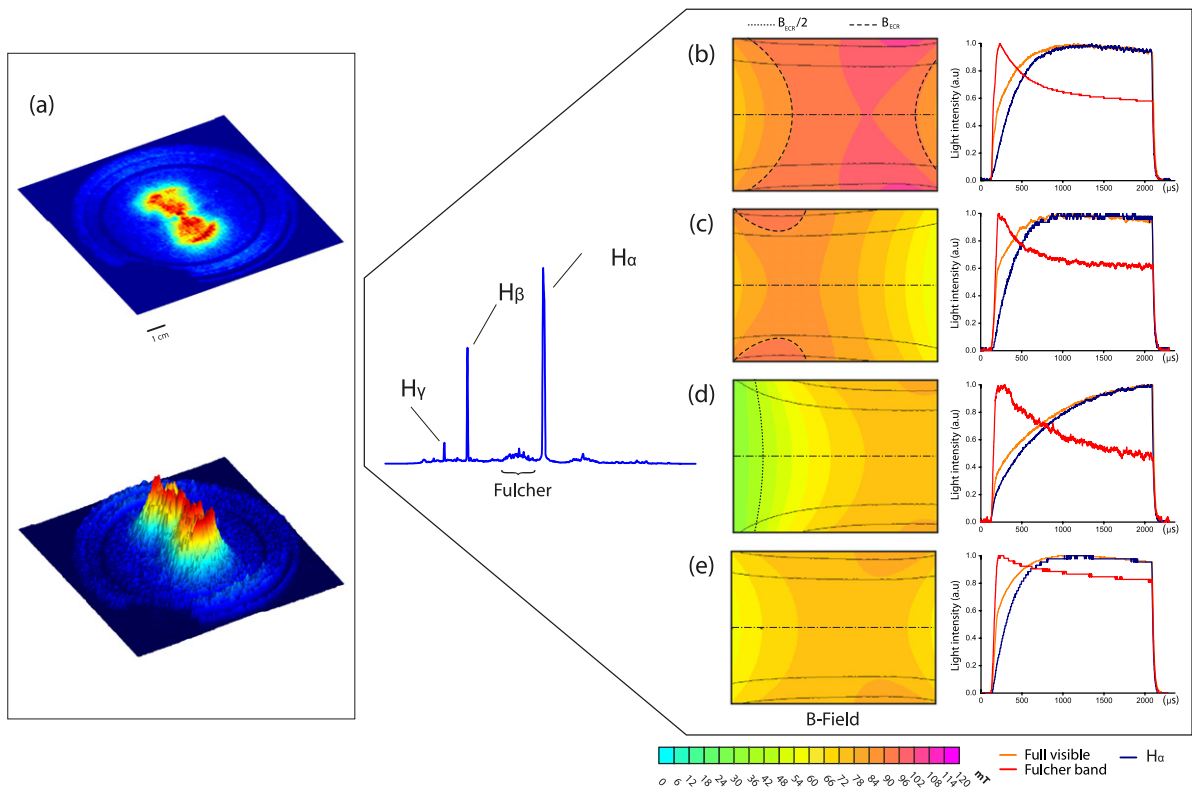

Figure 6. Hourglass shape recorded and its corresponding visible spectrum with magnetic field profiles where this shape is observed.

3.3. Slug

Figure 7(*a*) shows a typical plasma distribution denominated as *slug*. The slug shaped distribution is characterized by intense

light emission dominated by the Balmer-series. The temporal light emission is similar to the one obtained with the hourglass distribution. The magnetic field distribution resulting to the slug shaped light emission profile is typical for H^+ ion sources
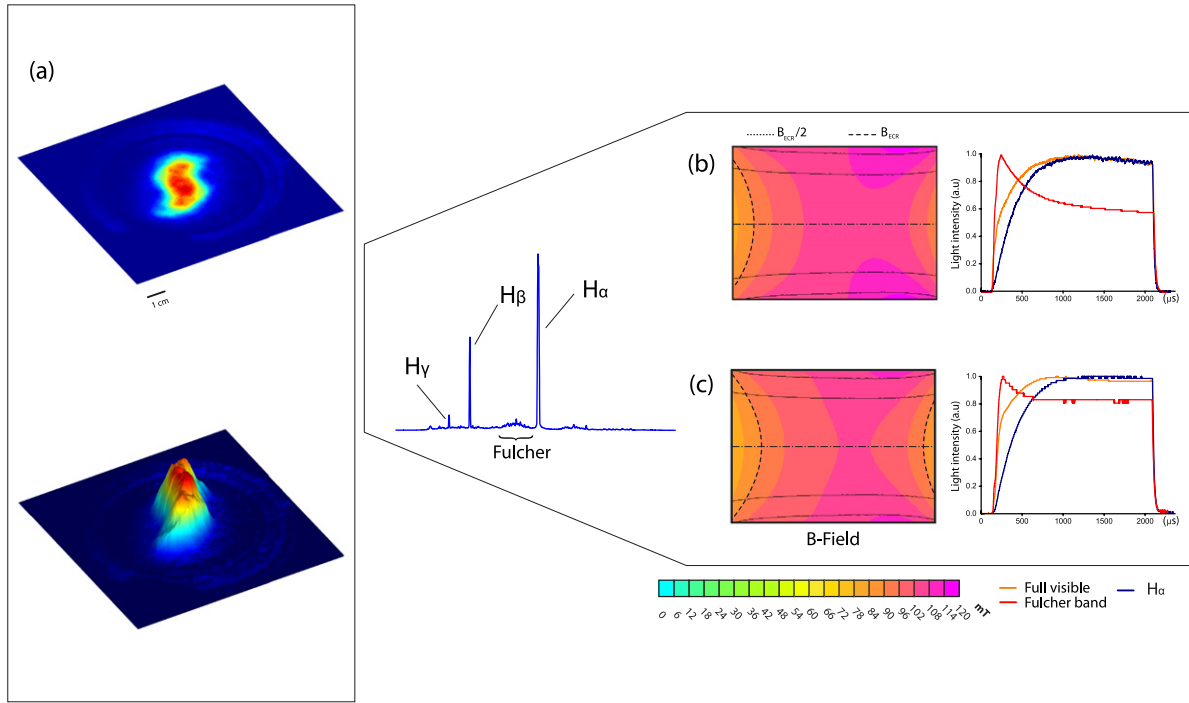
Figure 7. Slug shape recorded and its corresponding visible spectrum with the magnetic field profile where this shape is observed.
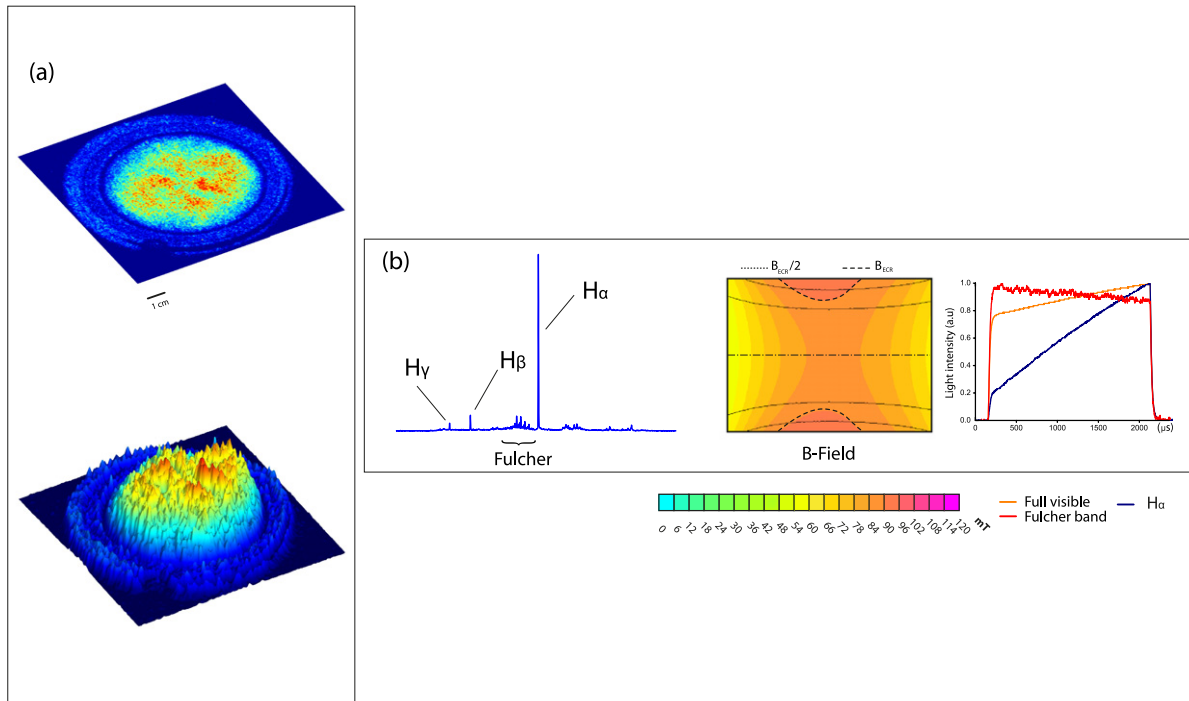

Figure 8. Flower shape recorded and its corresponding visible spectrum with magnetic field profiles where this shape is observed.

for which it has been observed to be beneficial to place the resonance surface in the close proximity of the microwave injection [8]. It has been observed that reversing the direction of the magnetic field causes the asymmetric slug to become mirrored with respect to the vertical axis i.e. the direction of the microwave electric field. The filtered light signals recorded with the slug distribution exhibit saturation times on the order of 0.5–1 ms.

3.4. Flower

Figure 8(*a*) shows a typical picture of the plasma distribution with four lobes, denominated as flower. This configuration is produced when the resonance surface does not span across the plasma chamber but instead forms a torus-like shape cut in half by the chamber walls. The visible light spectrum is dominated by the H_α line with monotonically increasing intensity throughout the microwave pulse. Altogether the
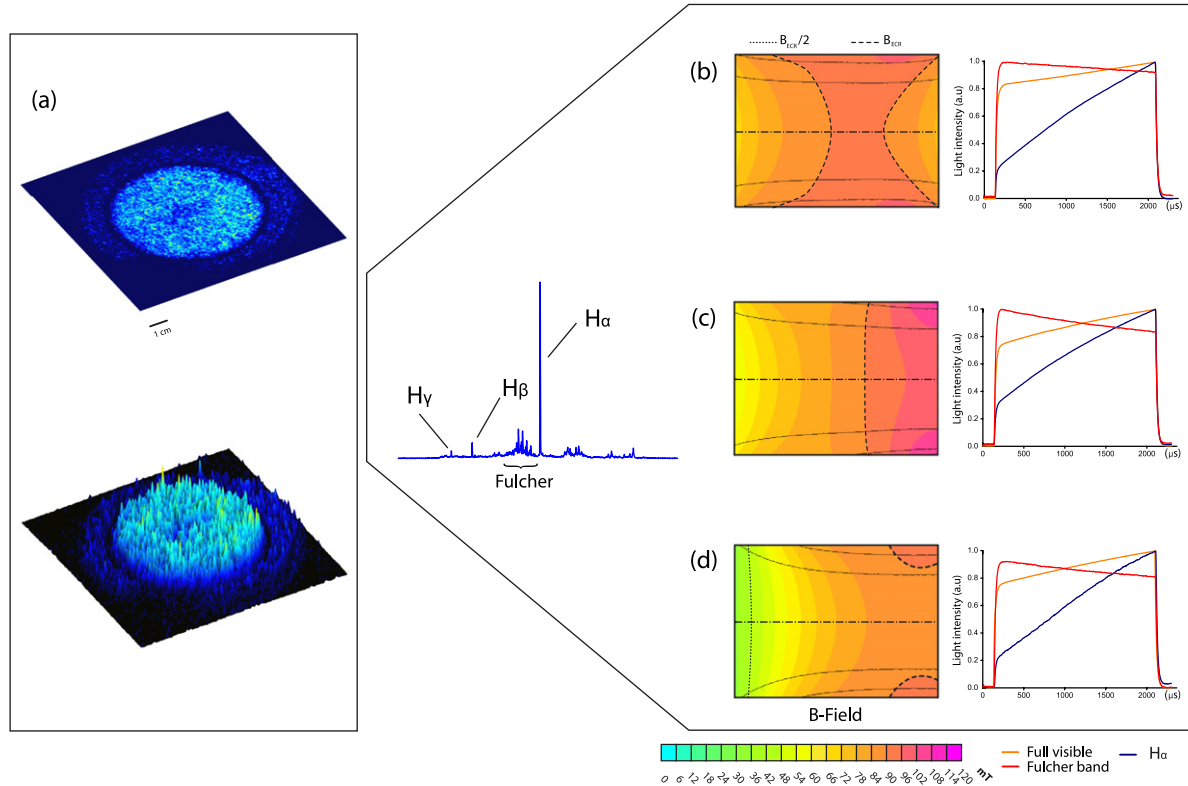
Figure 9. Full-chamber shape recorded and its corresponding visible spectrum with magnetic field profiles where this shape is observed.

intensity of the light emission is lower in comparison to the previous three distributions.

3.5. Full-chamber

Figure 9 shows a typical picture of practically homogeneous plasma distribution denominated as *full-chamber* The intensity of light emission is rather weak in this case. The only remarkable difference between the magnetic field profiles resulting to full-chamber or e.g. the slug is the distance between the microwave injection and the resonance surface. Steady-state light emission is not reached during the microwave pulse indicating a poorer microwave–plasma coupling in comparison to the slug distribution.

3.6. Ring

Figure 10(*a*) shows a typical picture of a thin layered plasma distribution near the chamber wall and denominated as ring. The corresponding 3D map of light intensity is shown in (*a*) lower picture and also the spectrum and its corresponding magnetic field distributions are also presented. The Ring distribution exhibits weak light intensity and is extremely sensitive to the magnetic field configuration.

3.7. Yin-Yang

Figure 11(*a*) shows a typical picture of a plasma distribution with an asymmetric lobe followed by a spiral-shaped tail. This distribution has been denominated as Yin-Yang. The given distribution is produced under specific off-resonance

magnetic field configuration. It has been observed that the Yin-Yang profile often rotates around the plasma chamber with a frequency of several kHz. Reversing the direction of the magnetic field reverses the orientation of the profile (similar to the other asymmetric case i.e. the slug) and the direction of the rotation.

3.8. Donut

Figure 12(*a*) shows a typical picture of a plasma distribution with a hollow profile, denominated as donut. The corresponding magnetic field configuration possesses a strong axial gradient with 50 mT at the injection and 120 mT at the diagnostics side. Thus, the ECR surface is embedded near the center of the plasma chamber.

4. Discussion

The presented study has provided evidence of various (eight) stable spatial plasma distributions in a 2.45 GHz microwave discharge, the magnetic field topology being the decisive factor separating them from each other. In general terms, the plasma distributions can be separated in two groups: high intensity emission exhibited by *column, hourglass* and *slug* and low intensity emission exhibited by *full-chamber, ring, flower, Yin-Yang* and *donut* configurations. Table 1 shows the relative light intensities recorded by the photodiode detector for all plasma modes and corresponding magnetic field profiles. The maximum intensity (100%) is recorded for the *column* distribution obtained with the magnetic field
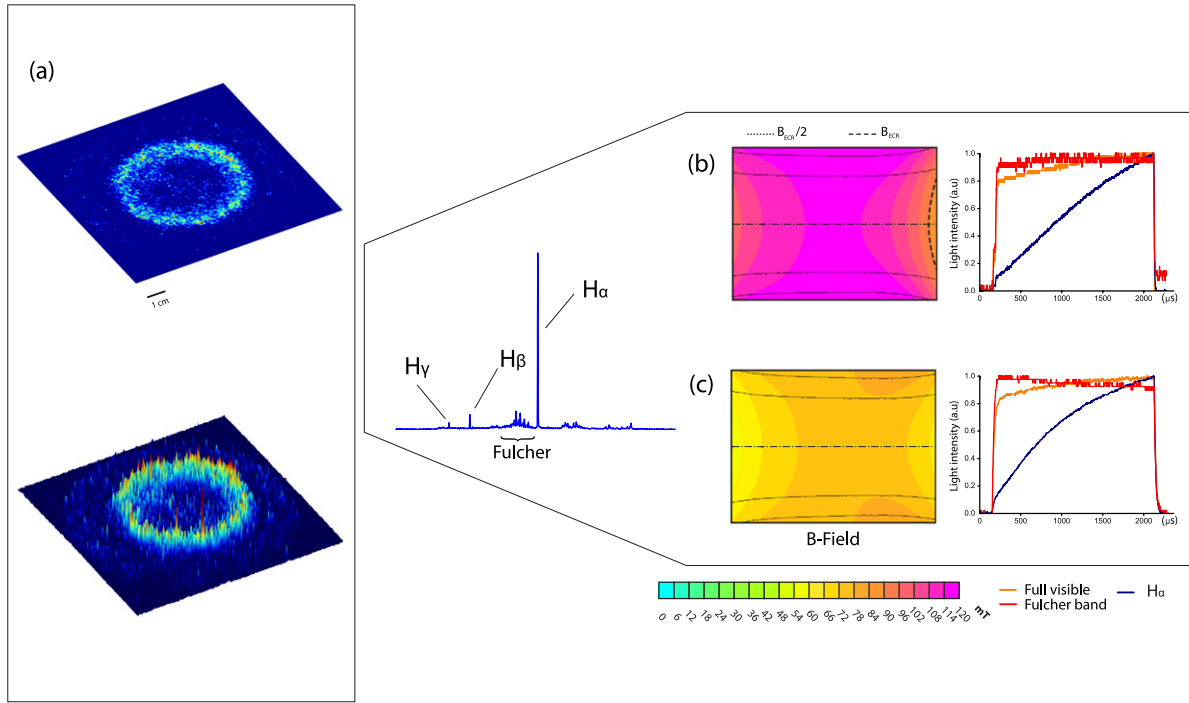
Figure 10. Ring shape recorded and its corresponding visible spectrum with magnetic field profiles where this shape is observed.
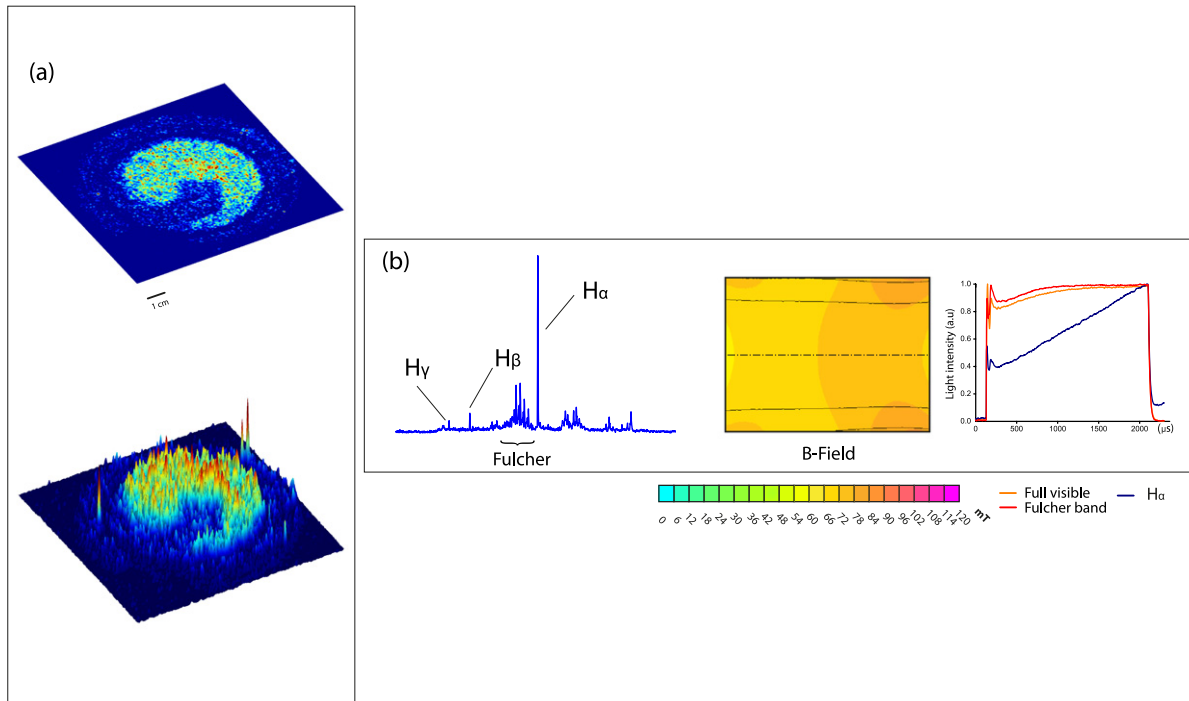

Figure 11. Yin-Yang shape recorded and its corresponding visible spectrum with magnetic field profiles where this shape is observed.

depicted in figure 5(*b*). The first three modes correspond to efficient microwave–plasma coupling with 75–90% of the incident power being absorbed by the plasma while the rest are characterized by a coupling of 5% or less. The microwave coupling characteristics of each distribution are also reflected in the temporal behavior of the filtered light signals. It is of note that none of the high-intensity profiles occupy the plasma chamber uniformly, which is often assumed to be the case for 2.45 GHz microwave discharges.

It is not evident why some magnetic field topologies fulfilling the resonance condition yield intense light emission (see figures 4(*a*)–(*c*)) while others fail in this respect (see figures 4(*d*)–(*h*)). In order to discuss possible reasons for the observed behavior we turn the attention into the electric field strength at the resonance. The strength of the electric
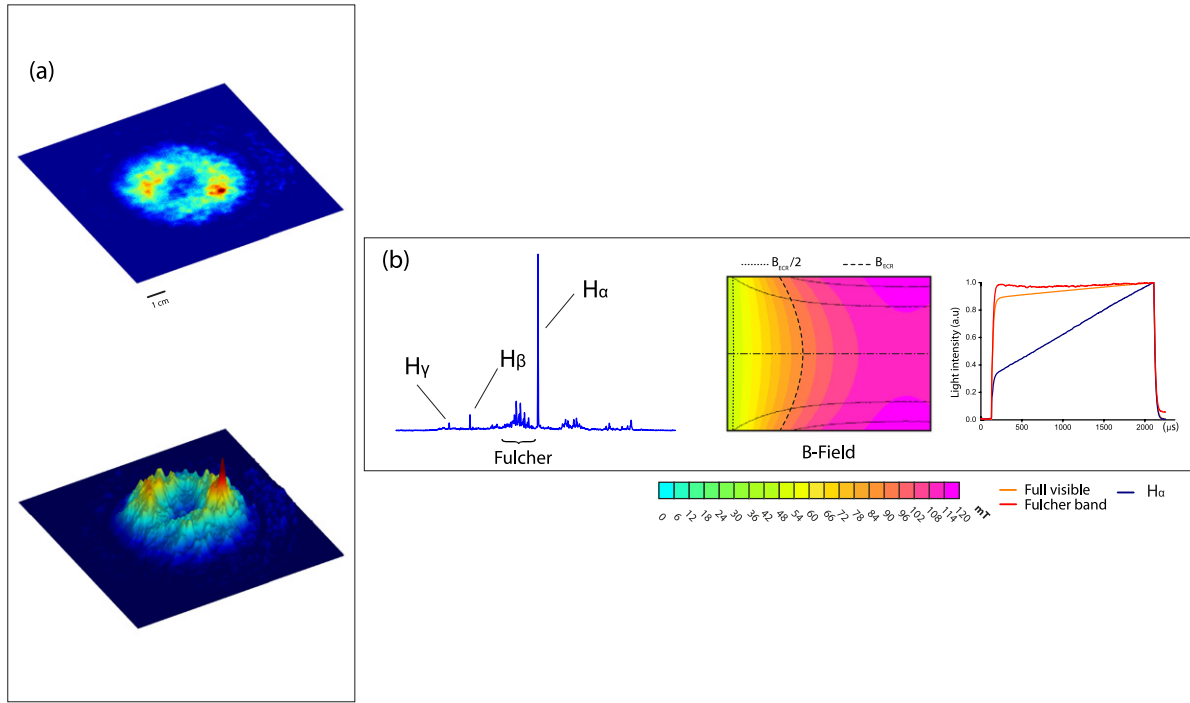
Figure 12. Donut shape recorded and its corresponding visible spectrum with magnetic field profiles where this shape is observed.

Table 1. Relative light intensity emissions for the observed distributions.

Mode	Mag. Field Fig.	Intensity (%)
Column	5(b)	100
	5(c)	50
	5(d)	3
Hourglass	6(b)	60
	6(c)	80
	6(d)	40
	6(e)	40
Slug	7(b)	60
	7(c)	80
Flower	8(b)	5
Fullchamber	9(b)	3
	9(c)	3
	9(d)	3
Ring	10(b)	3
	10(c)	3
YinYang	11(b)	3
Donut	12(b)	3

field is affected by the properties of the microwave coupling system [12] as well as propagation of the electromagnetic waves in the magneto-plasma. The electric field distribution of an empty plasma chamber is depicted in figure 13 showing a density plot of the time-averaged electric field strength and the direction of the oscillating field. It is worth noting that the light emission profiles corresponding to high intensity (see figures 4(*a*)–(*c*)) are aligned with the electric field. The plasma, however, affects the cavity properties and the electric field distribution [21]. This is because of different dielectric properties of the medium and damping of the propagating

microwave. It can be shown that RHCP waves can propagate in magneto-plasmas only if [22].

$$0 < \omega < \omega_{ce} \quad \text{or} \quad \omega > \frac{\omega_{ce} + \sqrt{\omega_{ce}^2 + 4\omega_{pe}^2}}{2} = \omega_{co}, \quad (1)$$

i.e. when the phase velocity of the incident wave is not imaginary. In the above equation $\omega_{pe} = \sqrt{\frac{n_e e^2}{\epsilon_0 m_e}}$ is the plasma oscillation frequency and ω_{co} the cut-off frequency. Due to the magnetic field topology it is assumed that the waves are propagating parallel to the external magnetic field, i.e. $\vec{k} \parallel \vec{B}_{ext}$. The resonance and cut-off magnetic fields for 2.45 GHz microwaves are plotted in figure 14.

If the incident wave propagates toward increasing magnetic field, which is the case for the TIPS plasma source, it reaches the cut-off before encountering the resonance and becomes evanescent. Under such condition resonant electron heating occurs only if the spatial distance z_e of the evanescent propagation from the cut-off to the resonance, is less than the skin depth $\delta \approx \frac{c}{\omega_{pe}}$. Thus, the condition for efficient energy transfer from microwaves to the plasma electrons can be written as

$$z_e < \delta + \frac{\Delta z}{2}, \quad (2)$$

where Δz is the effective resonance width [23] that can be expressed as

$$\Delta z \approx \sqrt{\frac{2\pi v}{\omega \frac{(\nabla B)_{ECR}}{B_{ECR}}}}, \quad (3)$$

where v is the electron velocity and ∇B the gradient of the magnetic field. At plasma densities of 1–5×10^{16} m^{-3}, typical for the TIPS plasma source [11, 12, 18], the skin depth for 2.45 GHz microwaves is 53–24 mm while the magnetic
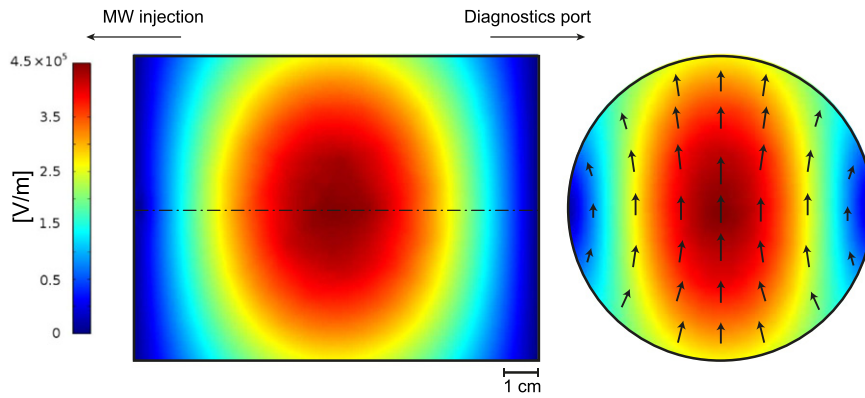
Figure 13. The electric field distribution of an empty plasma chamber simulated with COMSOL [20]. A density plot of the time-averaged electric field strength (left) and the direction of the oscillating field (right). The simulation takes into account the entire microwave system and plasma chamber.
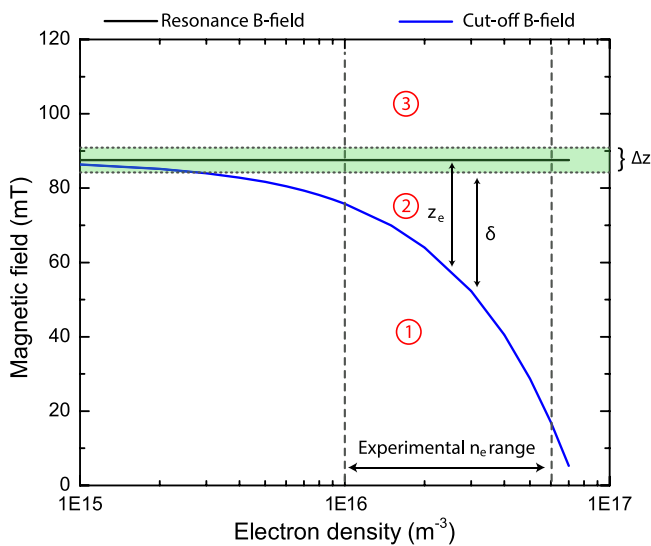

Figure 14. The resonance and cut-off magnetic fields as a function of plasma density for 2.45 GHz microwaves. RHCP-wave propagates in regions 1 ($\omega > \omega_{co}$) and 3 ($\omega < \omega_{ce}$). In region 2 the wave becomes evanescent and is attenuated. Resonant electron heating by microwaves launched toward increasing magnetic field occurs if the thickness of the evanescent region (z_e) is less than the skin depth (δ). In this generic representation, spatial distances Δz, z_e and δ are presented schematically in magnetic field scale since their actual values depend on electron (average) energy and magnetic field topology.

field gradient ranges from 0.3 to 1.0 T/m corresponding to an effective resonance width of 9–15 mm for 10 eV electrons (the order of magnitude of the average electron energy). Altogether, it can be estimated that the spatial distance between the cut-off and resonance fields should be less than ∼20–30 mm enabling efficient heating of the electrons. It is worth noting that equation (3) describes collisionless power absorption with the assumption that the transit time of an electron through the resonance is less than the average electron collision frequency. For the given parameters the electron transit time ($t_t = \frac{\Delta z}{v}$) through the resonance is on the order of 10^{-9} s while the average time between collisions is several orders of magnitude longer i.e. equation (3) is applicable.

The magnetic field topologies corresponding to intense light emission typically have the resonance surface spreading across the plasma chamber close to the injection. The magnetic field profiles corresponding to low light emission are either lacking the resonance surface or have a long distance from the injection to the resonance surface. This point is further highlighted in figure 15 comparing the light emission of two magnetic field topologies with identical neutral gas pressure and microwave power (6.2×10^{-3} mb and 2100 W). The resonance field gradient and maximum field are almost identical for these two profiles, the only remarkable difference being the distance between the boron nitride disk at the injection and the resonance surface. As discussed above, the distance from the injection to the resonance affects the propagation of the RHCP-component of the microwaves and sets an upper limit for the plasma density. For the magnetic field profile resulting to weaker light emission (on right in figure 15) it can be calculated that this limit is approximately $n_e = 3 \times 10^{16}$ m^{-3}. Above the given limit the evanescent region between the cut-off and resonance becomes thicker than the skin depth. It is of note that both the light emission profile and spectrum/intensity are affected by the spatial location of the resonance.

The magnetic field configurations resulting to different light emission profiles can be compared to the magnetic field profiles of high performance H$^+$/D$^+$ ion sources such as SILHI [24, 25] and LEDA [26, 27]. In the case of SILHI the microwaves are launched toward decreasing magnetic field which assures that they reach the resonance regardless of the plasma density i.e. the source can be operated in overdense mode. The optimum magnetic field profile of the LEDA ion source corresponds to the magnetic field profile resulting to the excitation of either column of slug mode (figures 5(*b*) and 7(*b*)). In these cases the microwaves are launched toward increasing magnetic field but they encounter the resonance surface in very close proximity of the microwave coupler and boron nitride disk enabling an efficient coupling of the microwave power even at high plasma density. Identifying the conditions (*B-field*, power and neutral gas pressure) corresponding to reproducible spatial distributions of the plasma allows linking them with ion currents and species
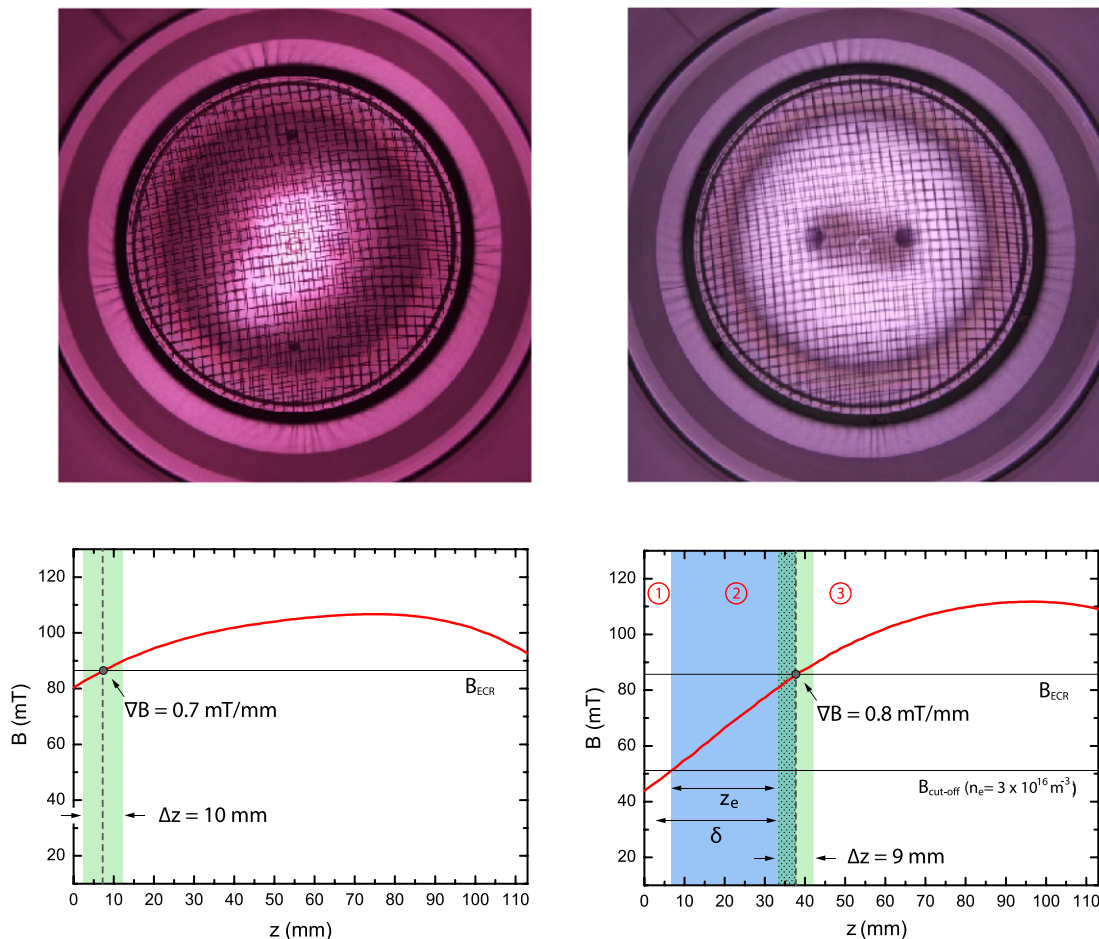
Figure 15. Light emission corresponding to two magnetic field profiles with different distances between the microwave injection and resonance. The calculated resonance width for 10 eV electrons and evanescent region at 3×10^{16} m^3 plasma density are shown in the plots depicting the on-axis magnetic field profiles.

fractions extracted from the TIPS plasma generator in the future.

References

[1] Pouzo J O, Milanese M M, Cortázar O D and Moroso R 2005 *IEEE Trans. Plasma Sci.* **33**

[2] Cortázar O D, Piriz A R, Prieto G R, Hoffmann D H H and Tahir N A 2008 *AIP Conf. Proc.* **996**

[3] Milanese M M, Cortázar O D, Moroso R, Nieldbaski J and Supán L 2011 *IEEE Trans. Plasma Sci.* **39**

[4] Okamoto A, Hara K, Nagaoka K, Yoshimura S, Vranges J, Kono M and Tanaka M 2003 *Phys. Plasmas* **10** 2211–6

[5] Biri S, Racz R and Palinakas J 2010 Studies of the ecr plasma in the visible light range *Proc. ECRIS 2010 (Grenoble, France)*

[6] Racz R, Biri S and Palanikas J 2011 *Plasma Sources Sci. Technol.* **20** 025002

[7] Nishino N, Nakashima Y, Higashizono Y, Kobashashi S, Islam K, Kubota Y, Yoshikawa M, Mishima Y and Cho T 2006 *Plasma Fusion Res.* **1** 035

[8] Gammino S, Celona L, Ciavola G, Maimone F and Mascali D 2010 *Rev. Sci. Instrum.* **81** 02B313

[9] Cortázar O D, Kompula J, Tarvainen O, Megías-Macías A, Vicaíno-de-Julián A and Koivisto H 2013 *Plasma Sources Sci. Technol.* **22** 015026

[10] Cortázar O, Megía-Macías A and Vizcaíno-de Julián A 2012 *Rev. Sci. Instrum.* **83** 3302

[11] Cortázar O, Megía-Macías A, Vizcaíno-de Julián A, Tarvainen O, Komppula J and Koivisto H 2014 *Rev. Sci. Instrum.* **85** 02A902

[12] Megía-Macías A, Cortázar O D and Vizcaíno-de Julián A 2014 *Rev. Sci. Instrum.* **85** 033310

[13] Behringer K and Fantz U 2000 *New J. Phys.* **2** 23

[14] Fantz U and Wűnderlich D 2006 *At. Data Nucl. Data Tables* **92** 853–973

[15] Janev R, Reiter D, Samm U and O M 2006 *J. Plasma Fusion Res. Ser.* **7** 319–22

[16] Verolainen Y and Nikolaich Y 1982 *Sov. Phys. USP* **25** 431

[17] Janev R, Reiter D and Samm U 2003 *Berichte des Forschungszentrums Jülich Technical Report* 4105 ISBN 0944-2952

[18] Cortázar O, Megía-Macías A and Vizcaíno-de Julián A 2013 *Rev. Sci. Instrum.* **84** 093301

[19] Meeker D 2010 Finite element method magnetics v4.2 www.femm.info

[20] 2013 Comsol multiphysics v4.2 www.comsol.com

[21] Lyneis C, Benitez J, Leitner D, Noland J, Strohmeier M, Koivisto H and Tarvainen O 2010 Characterization of the microwave coupling to the plasma chamber of the LBL ECR ion source *Proc. ECRIS 2010 (Grenoble, France)* pp 162–4

[22] Stix T H 1992 *Waves in Plasmas* (Berlin: Springer) ISBN 0883188597

[23] Williamson M, Lichtenberg A and Lieberman M 1992 *J. Appl. Phys.* **72** 3924–33

[24] Farchi A, Delaunay M, Melin G, Gobin R, Leroy P, Faure J, Delferrire O and Lagniel J 1996 *Rev. Sci. Instrum.* **67**

[25] Gobin R *et al* 2007 *High Energy Phys. Nucl. Phys.* **31** 46–50

[26] Sherman J D *et al* 2002 *Rev. Sci. Instrum.* **73**

[27] Vernon-Smith H, Schneider J and Sheffield R 2010 Low-energy demonstration accelerator (leda) test results and plans *Proc. 2010 Particle Accelerator Conf. (Chicago, IL)* pp 3296–8